ASME Open Journal of Engineering
Online journal at:
https://asmedigitalcollection.asme.org/openengineering

Mina Pakzadmanesh
Department of Bioengineering,
Northeastern University,
Boston, MA 02115
e-mail: pakzadmanesh.m@northeastern.edu

Samuel D. Salinas
Department of Bioengineering,
Northeastern University,
Boston, MA 02115
e-mail: salinas.s@northeastern.edu

Vineet S. Thomas
Department of Mechanical
and Industrial Engineering,
Northeastern University,
Boston, MA 02115
e-mail: v.thomas@northeastern.edu

Turner Jennings
Mem. ASME
Department of Mechanical
and Industrial Engineering,
Northeastern University,
Boston, MA 02115
e-mail: jennings.t@northeastern.edu

Hayden DelCiello
Khoury College of Computer Sciences,
Northeastern University,
Boston, MA 02115
e-mail: delciello.h@northeastern.edu

Ana I. Vargas
Mem. ASME
Department of Bioengineering,
Northeastern University,
Boston, MA 02115
e-mail: vargas.a@northeastern.edu

Julia Clarin
Mem. ASME
Department of Bioengineering,
Northeastern University,
Boston, MA 02115
e-mail: clarin.j@northeastern.edu

Rouzbeh Amini[1]
Mem. ASME
Department of Mechanical and Industrial
Engineering, Department of Bioengineering,
Northeastern University,
Boston, MA 02115
e-mail: r.amini@northeastern.edu

Mechanically Induced Deformation of Nuclei in the Tricuspid Valve Interstitial Cells: Experimental Measurements and Multi-scale Computational Simulation

We examined the mechanical deformation of valve interstitial cells (VICs) in the anterior leaflet of the tricuspid valve and explored the relationship between the extracellular matrix (ECM) structure and cellular mechanics. Fresh porcine hearts were used to prepare specimens, subjected to biaxial tensile testing, and imaged using confocal microscopy with VIC nuclei staining. A multi-scale computational framework was developed to analyze cellular deformation and orientation within the ECM, using nuclear aspect ratio (NAR) as a metric. Experimental results showed that NAR values increased with mechanical loading, from 2.57 ± 0.72 *in a traction-free state to* 3.4 ± 1.29 *at 130 kPa. Model predictions aligned with experimental findings. They also highlighted the significant impact of ECM fiber orientation on VIC nuclei deformation. These results indicate that mechanical forces profoundly influence cellular morphology and, potentially, their function. Further development of models is necessary to understand the complex interplay between the mechanical environment and cellular responses, crucial for identifying how mechanical forces affect tricuspid valve function and malfunction.* [DOI: 10.1115/1.4066002]

Keywords: mechanobiology, extracellular matrix, collagen, elastin, multi-scale modeling, homework

---

[1] Corresponding author.

Manuscript received June 7, 2024; final manuscript received July 12, 2024; published online August 13, 2024. Assoc. Editor: Hameed Metghalchi.

1 Introduction

The tricuspid valve (TV), located on the pulmonary side of the heart, ensures unidirectional blood flow from the right atrium to the right ventricle (Fig. 1). The TV function may be compromised, leading to a backward flow of blood from the ventricle to the atrium, known as tricuspid regurgitation. Whether occurring in isolation or alongside other valvular issues, tricuspid regurgitation is linked to a more than two-fold increase in cardiac mortality when left untreated [1,2]. However, surgical intervention on the TV, especially an isolated TV surgery, is often discouraged due to elevated in-hospital mortality rates ranging from 10% to 25% [3–6]. These sobering statistics, combined with our incomplete understanding of the pathogenesis of tricuspid regurgitation, underscore the importance of unraveling the mechanisms behind its development. Without elucidating such mechanisms, our capacity to establish precise patient selection criteria for surgery and to improve long-term outcomes remains limited.

Proper TV function relies on the biomechanical behavior of its three leaflets: the anterior, posterior, and septal leaflets. TV leaflets have complex microstructure that significantly affects the macro-scale biomechanical responses of the valve [7,8]. Specifically, proper coaptation of the leaflets, i.e., how the edges of the leaflets join together to close and seal the valve, is required for normal TV function. In atrioventricular valves, leaflet coaptation can be affected by changes in the mechanical integrity of the extracellular matrix (ECM) constituents, such as collagen and/or elastin [9]. Biomechanical remodeling of the ECM in TV leaflet may lead to valvular insufficiency and regurgitation [10]. For instance, Marfan syndrome is a genetic disorder characterized by an abnormal coding of the FBN1 gene for fibrillin-1. Fibrillin-1, part of the microfibril family that, in conjunction with an amorphous core made of elastin, constitutes the elastic fibers typically known as elastin [11–15]. While collagen provides structural stiffness to maintain leaflet coaptation during systole [16], elastin contributes long-range elastic properties such that the leaflet can recoil and extend during systole and diastole, respectively [11,16]. Marfan syndrome impacts 1 in every 3000–5000 individuals in the United States [17]. The mechanisms by which these genetically induced ECM changes affect the function of TV, especially in the context of tricuspid regurgitation induced by Marfan syndrome, remain poorly understood and warrant thorough investigation. Such a lack of knowledge is not unexpected, given that the TV has been referred to as the "forgotten valve" over the years [18].

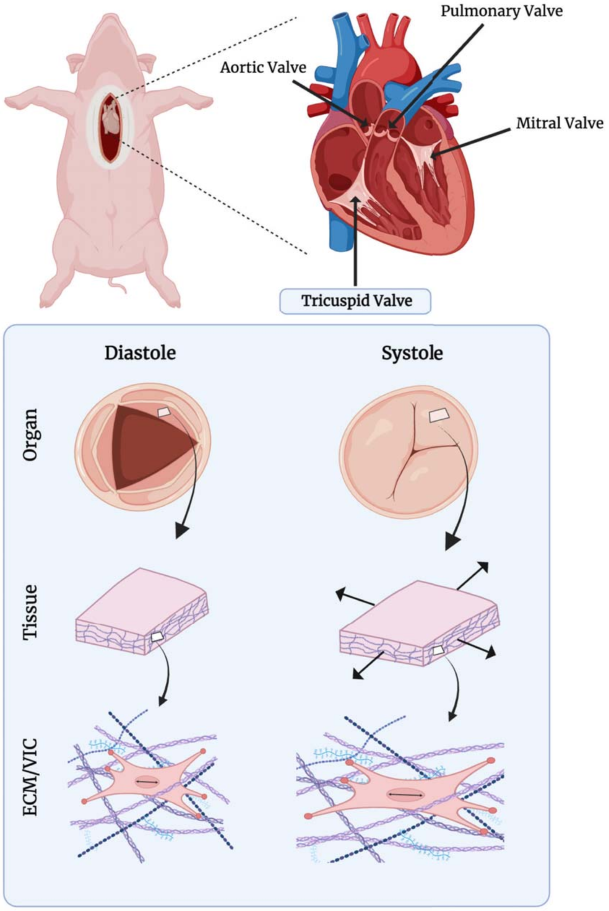

Fig. 1 Comprehensive illustration of cardiac structure and mechanical behavior during the cardiac cycle. The top panel illustrates the anatomy of the porcine heart TVs. The middle panel shows the TV transformation between diastole and systole. The lower panel details the corresponding microstructural changes in cardiac tissue and ECM/VIC interactions during the cardiac cycle. This image was created with BioRender.com.

The TV leaflets have a layer-like structure composed of the ECM and the residing valve interstitial cells (VICs) [19]. The VICs play a critical role in maintaining the mechanical integrity of the valve [20]. Among different functions, the VICs contribute to ECM protein synthesis and maintain a structurally competent leaflet. As such, it is important to identify changes in the biomechanical micro-environment of the TV interstitial cells in response to the ECM structural changes (Fig. 1). The VICs have the ability to sense its environment via mechanotransduction [21] and translate physical stimuli into biochemical activity that triggers intracellular signaling. This sensing mechanism is primarily initiated via fibrillar and focal adhesion points on the surface of the VICs [22]. Where fibrillar adhesions are small and/or elongated adhesion complexes, focal adhesions are much larger and contain cytoplasmic proteins (e.g., paxillin and vinculin) [23–25]. It is through the focal adhesion points on VICs that a robust anchorage to the ECM is made [23,25–29].

To the point that VICs respond via mechanotransduction, recent findings from Refs. [30,31] have documented that certain types of cells are able to sense confinement by means of nuclei deformation [30,31]. In addition, aortic valve interstitial cells have been found to respond to mechanical deformations. Ku et al. have documented that under sustained mechanical stretching, aortic VICs up-regulate the production of collagen type-III [32]. The physical stimuli that VICs receive may translate to different outcomes that may be tissue specific. In canine mitral valve, for instance, increased stretch (be it static or cyclic) has been found to induce cellular signaling that is favorable toward myxomatous pathology [33].

The objective of this study was to identify the relationship between the deformation of VICs—particularly that of VICs nuclei—and tissue-level mechanical loading. While existing computational models can capture the overall responses of the TV, they fall short in accurately predicting cellular deformation in response to changes of the ECM [7,34–38]. Prior experimental research has highlighted the variability of VIC nuclear shape in response to macro-scale mechanical loading in TV leaflets [36]. Our experimental/computational approach has helped us to extend such findings by identifying the correlation between the orientation of the ECM fibers and the nuclear shape in VICs of the TV. We examined cells in various alignments relative to the ECM fiber orientation, using a computational approach since such studies were not possible via experimental methods. Our computational scheme allowed for a more nuanced examination of how cellular orientation and ECM structure interplay in determining cell deformation and valve mechanics.

2 Methods

2.1 Experimental Measurements

2.1.1 Specimen Preparation. Fresh porcine hearts were acquired and delivered in phosphate buffered saline (PBS) to our facilities by a known provider of biological specimens (Animal

Technologies Inc., Tyler, TX). Once the hearts were received, the TV apparatus was located and the anterior leaflet was carefully isolated while maintaining some of the annulus for orientation purposes. This step allowed for differentiating the radial from the circumferential directions on the anterior leaflet specimen. Following the excision of the anterior leaflet, the specimens were kept at 4 °C until the time of mounting on a custom-made biaxial tensile machine. Details for the mounting procedure have been thoroughly explained in previous publications [39–44]. Briefly, the specimen was carefully sized and trimmed with the use of a tissue template that was placed such that the edges coincided with the radial and circumferential directions.

2.1.2 Specimen Fixation Under Mechanical Loading. Prior to mounting the specimen on the biaxial tensile machine, the thickness of the tissue was recorded using a leaflet gauge with a resolution of 0.001 in. (25.4 μm). The thickness of each specimen was used in determining, via the onboard software, the required equibiaxial load needed to achieve the following target equi-biaxial stress levels: 0, 5, 10, 40, 90, and 130 kPa. The tissue was mounted such that one axis of the specimen coincided with the radial direction, and the other axis with the circumferential direction of the leaflet. Once mounted, a total of ten preconditioning cycles were applied prior to specimen fixation in a bath of 4% paraformaldehyde in PBS. The biaxial tensile machine then executed a script that maintained the target stress level during the 2-h fixation process. Each fixation stress load included a sample size of 3, leading to a total count of 18 samples across all load levels. The samples were fixed under mechanical loading because the cross-linking of the ECM fibers due to fixation guaranteed that any morphological changes in the nuclei would be present after removal of the loads and during imaging as shown previously [45]. Following fixation, the samples were carefully removed and a surface sub-millimeter glass marker was attached to the top-right corner so as to establish orientation (radial from circumferential) for the forthcoming steps. In addition, a small notch was placed adjacent to the glass marker as a precautionary measure should the marker become dislodged. Specimens were subsequently stored in 70% ethanol.

2.1.3 Tissue Processing and Staining. Much the same with previous approaches [46,47], fixed specimens were processed and 20 μm-sections were obtained along the transmural-circumferential direction, coinciding with the bulk of collagen in the fibrosa layer of the leaflet. Following de-parafinazation, the sectioned tissue was permeabilized with Triton X-100 (Sigma Aldrich, SKU: X100-500ML), at a concentration of 1:1000, for 20 min, after which the VIC nuclei were stained with SYTOX Green (Thermo Fisher Scientific, Cat. No.: S7020) at 1:2000 for 15 min. The excess staining solution was then removed and the slide was mounted with Fluormount-G (Thermo Fisher Scientific, Cat. No. 50-187-88).

2.1.4 Image Acquisition and Processing. Specimens were imaged on a Zeiss LSM 880 having multi-photon capability with a Zeiss Plan-Apochromat 10×/0.45 objective. The stained VICs were imaged at an excitation wavelength of 504 nm, laser power set at approximately 1.5%, and the photomultiplier level at 550. The Z-stack acquired, throughout the thickness of the specimen, was captured at a resolution of 1024 × 1024 (16-bit).

Processing for the microscope images was carried out in IMARIS (Oxford Instruments, v. 9.9.0). Once the microscopy images were converted into native IMARIS format, the segmentation of VICs took place. In this step, VICs were identified as "Surfaces" and segmented with the background segmentation set at 7 μm and a seed point of 4.5 as a starting point. Seed placement was based on an "Intensity Mean" filter such that segmentation took place outward from the volume of higher average intensity of the stained VICs. After completing the segmentation wizard, further manual adjustments took place to ensure that the surface segmentation accurately represented that VICs in the Z-stack. Any surfaces segmented within 2 μm from the XYZ border was discarded so as to not include erroneous artifacts in subsequent analysis. A sample image set displaying native image acquisition with IMARIS-segmented surfaces can be seen in Fig. 2(*a*).

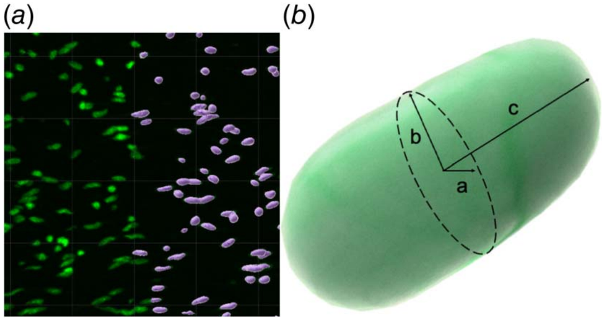

Fig. 2 **(*a*) Image data set showing stained VIC nuclei along with IMARIS-segmented surfaces and (*b*) a representative segmented VIC nuclei with the semi-axes notation *a*, *b*, and *c* used for nuclear aspect ratio calculation**

2.1.5 Nuclear Aspect Ratio Calculation. Data were exported from IMARIS and processed with a custom script in MATLAB (Mathworks Inc., Natick, MA). Among the metrics exported from IMARIS were the vectors for each axis of each of the segmented VICs. From there, in order to obtain the nuclear aspect ratio (NAR), as a measure nuclear deformation [45,48], the following equation was used.

$$\mathrm{NAR} = \frac{\|\boldsymbol{c}\|}{\|\boldsymbol{a}\|} \tag{1}$$

where $\boldsymbol{c}$ the largest axis vector and $\boldsymbol{a}$ the smallest axis vector were generated by IMARIS based on a fitted ellipsoid of each segmented surface. This calculation was carried out to acquire an overall NAR for the imaged sample.

2.1.6 Leaflet Mechanical Testing and Structural Analysis of the Underlying Extracellular Matrix. Data on macro-scale mechanical responses of the tissue and the underlying structure of the ECM were necessary inputs for the computational model. As such, we performed the following experiments on a selected fresh anterior leaflet. We first used our custom-made biaxial testing device to identify the tension/deformation responses of the tissue as described in detail previously [39–44]. The specimen was subsequently unmounted from the biaxial testing equipment once the data were recorded and then mounted on a small angle light scattering (SALS) device for imaging purposes [7,8,49–51]. The experimental method of SALS is provided in our previous publications [7,8]. Briefly, a 5 mW He–Ne laser beam (Model 1125) with random polarization passed through the sample, scattering off the fibrous structures. The scattering pattern was captured by a digital camera (Grasshopper3 2.3 MP Mono USB3 Vision, GS3-U3-23S6M-C) placed behind a Mylar screen. Each fiber bundle contributed its scattered light intensity at an angle of $\theta + 90$ deg, as the pattern was perpendicular to the fiber direction θ. The post-processed SALS scan output was employed to generate a second-order orientation tensor H_{ij} [52,53]:

$$H_{ij} = \oint r_i r_j R(\theta) d\theta \tag{2}$$

where θ is the fiber direction, $R(\theta)$ is the fiber distribution function obtained from SALS, and r_i is a unit vector in the direction of θ

defined by

$$
\begin{aligned}
r_1 &= \cos\theta \\
r_2 &= \sin\theta
\end{aligned}
\tag{3}
$$

From the eigen analysis of H_{ij}, we obtained

$$H_{ij} = \lambda^{(1)}\left(w_i^{(1)}w_j^{(1)}\right) + \lambda^{(2)}\left(w_i^{(2)}w_j^{(2)}\right) \tag{4}$$

where $w_i^{(k)}$ and $\lambda^{(k)}$ are the eigen vectors and eigen values of H_{ij}, respectively. Note that $\lambda^{(2)} \geq \lambda^{(1)}$. The anisotropy index, α, a measure of ECM network spread, and the main fiber direction, μ, were then defined by

$$\alpha = \left(1 - \frac{\lambda^{(1)}}{\lambda^{(2)}}\right) \times 100\% \tag{5}$$

$$\mu = \tan^{-1}\left(\frac{\mathbf{w}^{(2)} \cdot \mathbf{e}_2}{\mathbf{w}^{(2)} \cdot \mathbf{e}_1}\right) \tag{6}$$

where $\mathbf{e}_1$ and $\mathbf{e}_2$ were the unit vectors in the horizontal and vertical directions of the scanned image (corresponding to circumferential and radial anatomical directions), respectively.

2.2 Computational Modeling

2.2.1 Multi-scale Finite Element Model. In this study, we employed a multi-scale model approach originally developed for analysis of collagen gels [54]. This model, used in a range of fibrous soft tissues and biomaterials, has been described in detail previously [55–57,51,7,58–62]. Briefly, each finite element included eight Gauss points, with individual representative volume elements (RVEs) positioned at each Gauss point (Fig. 3). The macroscopic volume-averaged Cauchy stress S'_{ij} was generated by the RVE boundary deformations, which caused the RVE network to rearrange and deform. This process was reflected in the microscopic stress tensor s'_{ij} at each integration point within each finite element using a volume averaging approach [63].

$$S'_{ij} = \frac{1}{V'}\int_V s'_{ij}\,dV \tag{7}$$

$$S'_{ij} = \frac{1}{V'}\sum_{\text{boundary crosslinks}} x'_i f_j \tag{8}$$

where x'_i represents the i^{th} component of the position at the boundary cross-link (i.e., on one of the six edges of the RVE) and f_j denotes the force exerted on the boundary cross-link in the j-direction. An undeformed RVE embodied a computational space with a dimensionless unit measure [55]. The conversions of $V' = \gamma^3 V$ and $x'_i = \gamma x_i$ enabled the representation of the physical space of the tissue using the unit computational domain. The scaling parameter γ denotes the edge length of the RVE at the tissue level (i.e., physical domain), resulting in a total fiber length of γL, with L being the total length of fibers in the computational domain. Consequently the total (actual) fiber volume was $\gamma L A_f$, with A_f representing the mean cross-sectional area of all fibers. The volume fraction ψ was expressed by dividing the total volume of the fibers, $\gamma L A_f$, over total volume of the undeformed RVE, γ^3 [7]:

$$\psi = \frac{LA_f}{\gamma^2} \tag{9}$$

The volume fraction (a property of the network that is experimentally measured) was related to the computational values of the RVE (i.e., x_i and V) and the volume-averaged Cauchy stress tensor S'_{ij} was achieved [54]:

$$S'_{ij} = \frac{\psi}{LA_f}\frac{1}{V}\sum_{\text{boundary crosslinks}} x_i f_j \tag{10}$$

The fibers within the model were represented as nonlinear springs, where the force f in the fibers followed a nonlinear constitutive equation [64] for as long as the fiber stretch λ_f remained below a critical stretch value of λ_f^c. Once the critical stretch value of λ_f^c was surpassed, the fiber was modeled as a linear spring:

$$f = \begin{cases} \frac{E_f A_f}{\beta}\left(e^{\beta\varepsilon_G} - 1\right), & \lambda_f < \lambda_f^c \\ \frac{E_f A_f}{\beta}\left(e^{(\beta\varepsilon_G^c)} - 1\right) + E_f A_f \lambda_f^c e^{(\beta\varepsilon_G^c)}\left(\lambda_f - \lambda_f^c\right), & \lambda_f > \lambda_f^c \end{cases} \tag{11}$$

where $\varepsilon_G = (1/2)(\lambda_f^2 - 1)$ is the fiber Green strain, ε_G^c is the strain value when the stretch reaches the critical value of λ_f^c, E_f is a parameter that relates to the fiber stiffness with the same dimension as elastic modulus, and β is a dimensionless parameter representing the nonlinearity of the force response.

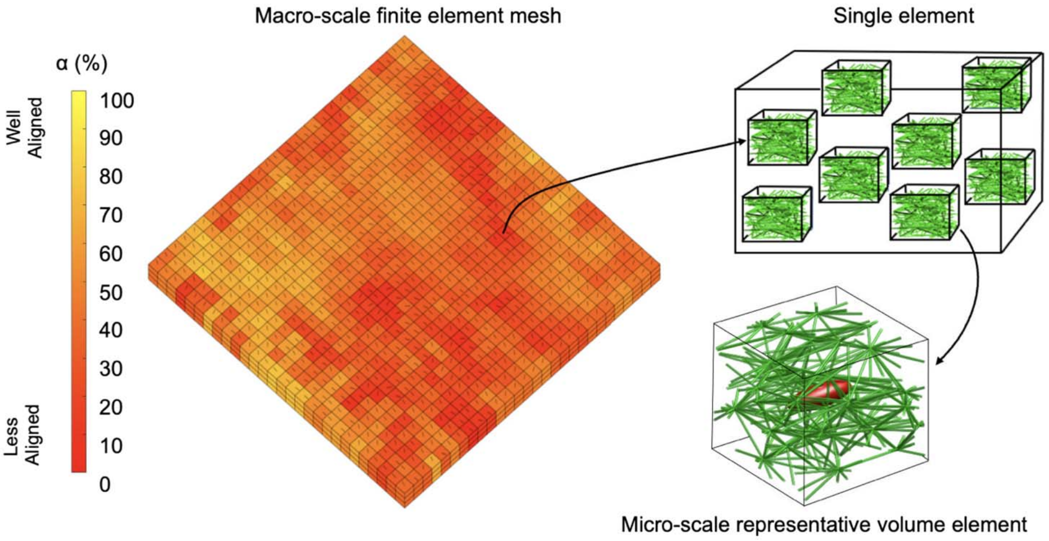

Fig. 3 Diagram illustrating the model. Cell nuclei were represented as ellipsoids. Deformation of these ellipsoids resulted from the rotation and stretching of extracellular matrix fibers within the micro-scale representative volume element and the NAR was calculated for various macro-scale loading levels.

The stress contribution arising from the non-fibrous matrix, denoted as S^m_{ij}, was determined using a neo-Hookean model [65]:

$$S^m_{ij} = \frac{G}{J}\left(B_{ij} - \delta_{ij}\right) + \frac{2G\nu}{J(1-2\nu)}\ln(J)\delta_{ij} \tag{12}$$

with B_{ij} being the left Cauchy green deformation tensor at macro-scale, J being the determinant of the deformation gradient tensor F_{ij}, G being the shear modulus, and δ_{ij} being the Kronecker delta. The parameter ν serves as a material constant which, in the linear elasticity range, corresponds to the Poisson's ratio. As demonstrated earlier, employing the Poisson's ratio as a material parameter in the initial configuration enables the assumption of nearly incompressible material behavior when ν approaches a value of 0.5 [66–68]. The stress contribution originating from the non-collagenous matrix was considered to exhibit variations solely on the macroscopic scale. Microscopic equilibrium $\left(s'_{ij,i} = 0\right)$ was presumed, and the Leibnitz theorem was employed to derive the divergence of the macroscopic stress tensor [54]:

$$S'_{ij,i} + S^m_{ij,i} = \frac{1}{V}\oint_{\partial V}\left(s'_{ij} - S'_{ij}\right)u_{k,i}n_k dA \tag{13}$$

where $u_{k,i}$ is the gradient of the displacement u at the surface and n_k is the normal to the surface of the RVE. To solve the macroscopic boundary value problem, the deformation of the RVE boundaries was first determined using the macroscopic deformation field. Then, the fiber force balance was computed for each RVE. The volume-averaged Cauchy stress of the ECM fibers was determined and subsequently applied in a macroscopic stress balance equation, which was solved through an iterative process. The solution involved iterating between the nonlinear macroscopic finite element problem and the microscopic force balance using the Newton–Raphson method until convergence was achieved [7].

Three-dimensional fiber networks for each RVE were generated to match experimental data obtained from SALS as described in detail previously [7]. At the tissue level, the model was discretized into 2352 macro-scale elements in three layers along the thickness. Each RVE was composed of approximately 450 micro-scale elements. As such the model had a total of $\sim 10^8$ degrees-of-freedom. Similar to our previous work [7], the load-control biaxial experimental data of the leaflet were then used to estimate the model parameters: $G = 2.0\,\text{kPa}$, $E_f = 20\,\text{kPa}$, $\lambda^c_f = 1.1$, and $\beta = 89.7$ (Fig. 4). The coefficient of determination R^2 was utilized to evaluate the agreement between the finite element model and equibiaxial experimental data:

$$R^2 = 1 - \frac{\sum_{i=1}^{n}\left(y_i - \hat{y}_i\right)^2}{\sum_{i=1}^{n}\left(y_i - \bar{y}\right)^2} \tag{14}$$

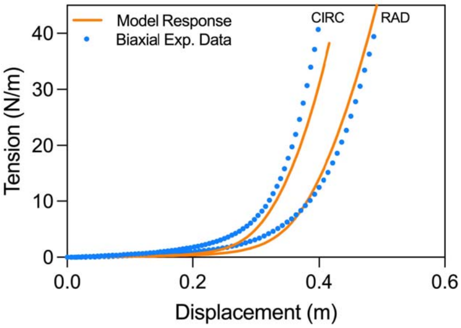

Fig. 4 Simulated multi-scale model response after fitting the model parameters to equibiaxial data measured using biaxial tensile testing equipment ($R^2 = 0.94$)

where y_i represents the experimental data, $\bar{y}$ denotes the mean of y_i, and $\hat{y}_i$ represents the values obtained from the simulated model.

2.2.2 Computational Estimation of Valve Interstitial Cell Nuclear Deformation. An approximation of the complex cell–ECM fiber matrix mechanism was considered as our VIC deformation model. Mechanical stresses are transmitted to the cell nuclei from the ECM fibers through a sophisticated network involving focal adhesions and intracellular structures. Focal adhesions serve as the connection points between cells and the external ECM at the cell membrane, facilitated by transmembrane proteins known as integrins [29]. Omitting the intricate intracellular structural components, we developed a representative model to predict the nuclear deformation in coordination with the deformation of the fiber network in response to applied macro-scale loading.

An ellipsoidal geometry was assumed for the cell nucleus [69]. The center of the ellipsoid was positioned within the geometric center of the RVE in the undeformed configuration. The change of the ellipse aspect ratio was used as a measure of the cellular deformation similar to the NAR calculation described in Eq. (1). The following mathematical equation was used to express the ellipsoids in quadratic forms [70]:

$$(\hat{x}_i - v_i)D_{ij}(\hat{x}_j - v_j) = 1, \quad D_{ij} = Q_{ik}Q_{jl}\Lambda_{kl} \tag{15}$$

$$\left[\Lambda_{ij}\right] = \begin{bmatrix} \frac{1}{\|\boldsymbol{a}\|} & 00 & \\ 0 & \frac{1}{\|\boldsymbol{b}\|} & 0 \\ 0 & 0\frac{1}{\|\boldsymbol{c}\|} & \end{bmatrix} \tag{16}$$

$$\left[Q_{ij}\right] = \begin{bmatrix} V^{(1)}_1 & V^{(2)}_1 & V^{(3)}_1 \\ V^{(1)}_2 & V^{(2)}_2 & V^{(3)}_2 \\ V^{(1)}_3 & V^{(2)}_3 & V^{(3)}_3 \end{bmatrix} \tag{17}$$

where $\hat{x}_i$ is the position of each point on the surface of the ellipsoid, and v_i is a vector that identifies the center of the ellipsoid. In Eq. (15), D_{ij} represents a positive definite, real, symmetric matrix, with eigenvectors $V^{(i)}_k$'s corresponding to the ith semi-axes of the ellipsoid. Furthermore, $\|\boldsymbol{a}\|$, $\|\boldsymbol{b}\|$, and $\|\boldsymbol{c}\|$ used in Eq. (16) are the lengths of the semi-axis of the ellipsoid. Using the results of our multi-scale finite element model described above, the following steps were performed to calculate the computational estimation of NAR:

(1) The initial lengths of the semi-axes $\boldsymbol{a}$, $\boldsymbol{b}$, and $\boldsymbol{c}$ in the undeformed configuration were chosen based on the experimentally measured NARs (as described above), at the traction-free (referential) configuration.

(2) For any RVE used for this calculation, the vector v_i was chosen as the position vector of the center of RVE at the stress-free configuration. Unless otherwise specified, the semi-axes of the ellipsoid ($V^{(i)}_k$'s) were chosen in such a way that the largest axis was aligned with the main fiber direction of each RVE at the stress-free configuration [43]. Choosing a single ellipsoid in any of the RVEs was justified based on the geometric and scaling parameters used in the multi-scale model. In particular, while RVEs were generated in a $1 \times 1 \times 1$ computational domain, the length of fibers and the size of the nucleus were scaled using fiber diameter equal to 450 nm [71], and volume fraction ψ equal to 0.43 [72]. Based on the physical size of RVE edge length (computed as $\gamma = \sqrt{LA_f/\psi} = 12.6\ \mu\text{m}$, where L is 101 and A_f is $3.925 \times 10^{-07}\ \text{mm}^2$) and the averaged measurements of the major and minor axes length obtained from confocal microscopy images (and the subsequent analysis in IMARIS), we were able to locate at least one nucleus in each RVE.

Table 1 Different configurations of the fiber network and nucleus in four scenarios (mean ± standard deviation)

Scenario	Number of chosen networks	Initial NAR	Total number of cell modeled	Orientation of nuclei	μ
I	1	2.57	80	59 deg ± 42 deg	59 deg
II	1	2.57 ± 0.73	80	In alignment with μ	59 deg
III	80	2.57	80	In alignment with μ	59 deg ± 40 deg
IV	80	2.57 ± 0.71	80	59 deg ± 41 deg	61 deg ± 42 deg

(3) At the stress-free configuration, the intersection of the ellipsoid with eight randomly chosen fibers were identified and used as eight points representing the location of eight focal adhesion points.

(4) At each deformed state of the RVE obtained from the multiscale model, the deformed positions of the eight focal adhesion points were obtained simply by identifying their location relative to the deformation of the two ends of the deformed fiber to which they belonged.

(5) The updated position of the eight focal adhesion points, along with the assumption that the volume of the ellipsoid was unchanged during process of deformation, were used to obtain a new ellipsoid using Eq. (15) and via Newton–Raphson's iterative method. In particular, to define an ellipsoid in the deformed configuration, we needed to find the position of the center of the deformed ellipsoid v_i (three unknowns), and the six parameters necessary to define the symmetric matrix D_{ij}. Equation (15) for the deformed position of each focal adhesion point gave us a single independent equation (i.e., total of eight independent equations) which along with the assumption of incompressibility were enough to find the unknowns via a system of nonlinear algebraic equations.

(6) The updated NAR for each loading step were then calculated using parameters of the new ellipsoid at each deformed configuration.

To evaluate changes in the response of the nuclei of TV interstitial cells to macro-scale equibiaxial mechanical loading, as predicted by our nuclear deformation model, numbers of fiber networks were randomly selected from three layers of the TV anterior leaflet. We determined the changes in the NAR under equibiaxial mechanical load in four different scenarios in initial configurations (Table 1):

(i) A single representative fiber network, wherein nuclei with the same initial NAR value (2.57, identified as the average of microscopy data) was oriented in 80 different directions relative to the network.

(ii) A single representative fiber network, encompassing nuclei with 80 different initial NAR values but all aligned with the main fiber direction of the fiber network.

(iii) A total of 80 fiber networks with nuclei of the same initial NAR value (2.57) aligned with the mean fiber directions of their respective encompassing fiber network.

(iv) A total of 80 fiber networks with various initial NAR and random cell alignments relative to the mean fiber orientation.

3 Results

Based on microscopy and subsequent image analysis, the average NAR of the overall population of segmented VIC nuclei exhibited an upward trend as mechanical loading increased. The NAR values, starting from the traction-free state to the highest loading conditions, were 2.57 ± 0.72 (mean ± standard deviation), 2.45 ± 0.70, 3.13 ± 1.21, 2.81 ± 0.91, 3.19 ± 1.14, and 3.4 ± 1.29 for 0, 5, 10, 40, 90, and 130 kPa loading conditions, respectively. Microscopy also showed that VIC nuclei are predominantly circumferentially oriented, aligning with the primary fiber direction in the valve leaflet, albeit with some deviations in out-of-plane directions (data not included).

As shown in Fig. 4, and similar to our previous published works [7,51], we were able to fit the experimentally obtained mechanical testing outcomes to the micro-structurally accurate multi-scale model reasonably well ($R^2 = 0.94$). Figure 5 displays the undeformed and deformed configurations of the finite element model under two levels of equibiaxial loading conditions. Additionally, it demonstrates the changes in NAR within a representative fiber network when subjected to various mechanical loads. It should be noted that the nucleus in this specific case was aligned with the main fiber direction in the undeformed configuration.

Figure 6 shows how NAR alterations were apparent under increasing stress levels in all four tested scenarios as compared to

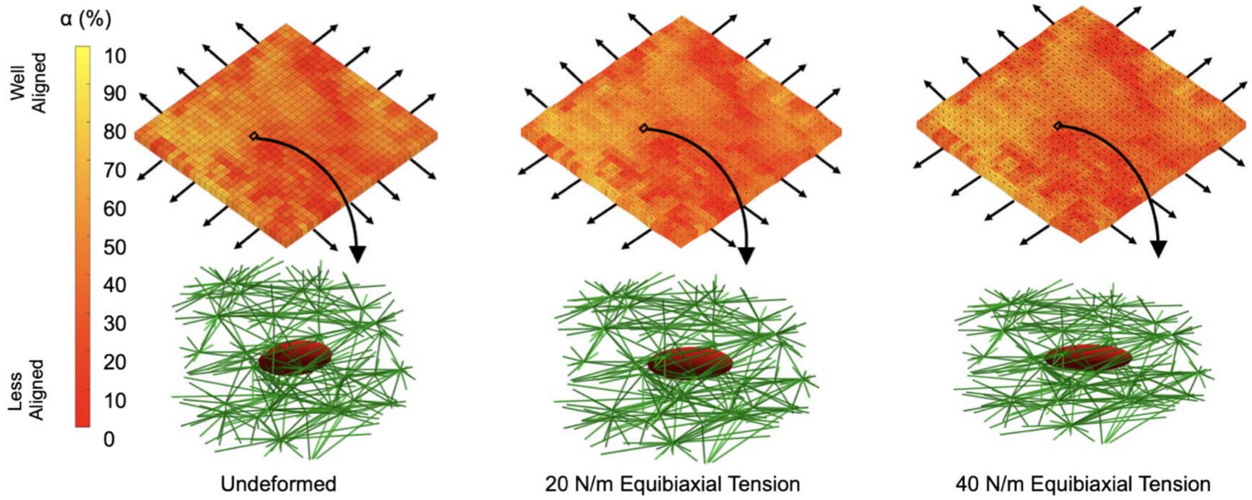

Fig. 5 Comparison of the undeformed and deformed states of the finite element model under different equibiaxial loading conditions. Each configuration shows the effect of fiber stretching on the deformation of a representative embedded ellipsoid-shaped cell nucleus. The cell nucleus was positioned to align with the mean fiber direction of the network at the initial undeformed configuration.

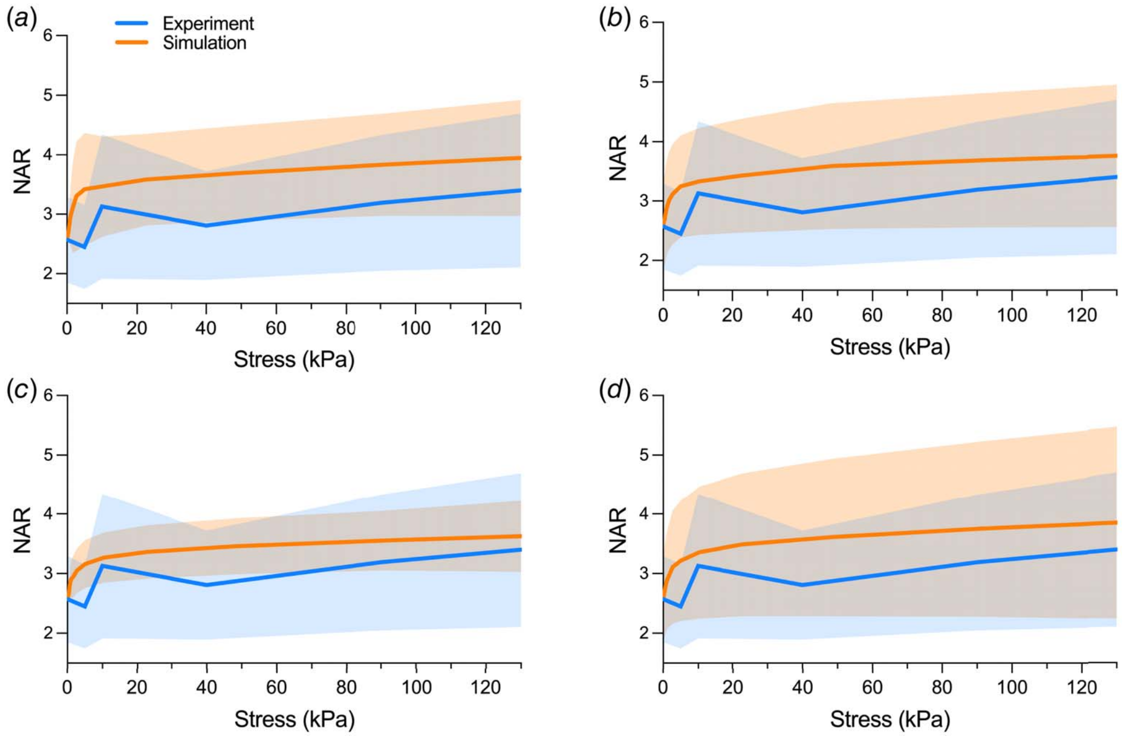

Fig. 6 Variations in NAR under equibiaxial mechanical loading across four scenarios. (*a*) Scenario I represents a fiber network with cell nuclei oriented in 80 different alignments relative to the mean fiber direction. (*b*) Scenario II features a network where cell nuclei have 80 different initial NAR values. (*c*) Scenario III represents 80 fiber networks with different alignments, with an identical initial NAR of 2.57 aligned with the main fiber direction of each network. (*d*) Scenario IV represents 80 fiber networks with variable nuclei alignment relative to the mean fiber orientation and variable initial NARs. Shaded regions represent standard deviation.

the measurements obtained experimentally. Figure 6(*a*) illustrates changes in NAR that occur at various loading levels when the nucleus are oriented at different angles relative to the mean fiber direction (scenario I). Our model response revealed an increase in NAR, increasing from 2.57 to 4.00. Notably, the computational findings align consistently within the experimentally measured values, and the model response mainly falls within the standard deviation of the experimental finding.

Figure 6(*b*) shows the model response under different loading levels in one representative fiber network (scenario II), where initial NAR varied between 1.33 and 4.69. The mean NAR values increased from 2.57 to 4.27 under the increase in loading level from 0 to 130 kPa. Additionally, the results obtained from the computational model has the same increasing trend as those values measured through microscopy. As shown in Fig. 6(*c*), similar trend was observed in scenario III (i.e., nuclei in 80 fiber networks all with the same initial NAR value of 2.57) where NAR increased with rising stress levels with an increase in NAR from 2.57 to 3.66.

The mean NAR values of randomly oriented nuclei in relation to the mean fiber direction of 80 different networks (scenario IV) are shown in Fig. 6(*d*). A rapid initial rise in the NAR followed by a continued increase but at a reduced rate (increasing from 2.57 to 3.91) is shown in Fig. 6(*d*). The predictions of the computational model under scenario IV further increased our confidence in its capability for investigating the biomechanical behavior of nuclei in fiber networks subjected to various loading conditions. As shown in Fig. 6(*d*), the model responses matched the trend observed in experimental findings.

4 Discussion

Research on the TV has traditionally been overshadowed by more extensive studies on the aortic and mitral valves, largely due to the greater prevalence of left heart diseases that involve these latter valves. [18,73]. However, with the increasing focus on right heart disease, the significance of tricuspid valve disease as a major contributor to morbidity and mortality is now being acknowledged [74–76]. In the realm of biomechanics, many researchers in recent years have extensively examined the structure, function, and malfunction of TV [36,77–81]. A pivotal aspect in advancing our comprehension of tricuspid valve disease involves distinguishing the connection between the microstructure of the tissue and the mechanics of the leaflets, initially in a healthy state and subsequently in disease.

The findings of this study provide valuable insights into the intricate relationship between VIC nuclear deformation and tissue-level mechanical loading within the TV complex. By leveraging a combined experimental and computational approach, we were able to elucidate the correlation between ECM fiber orientation and nuclear shape in VICs. Although research on the mechanobiology of VIC nuclei in relation to macro-scale loading in both healthy and diseased hearts is scarce, the importance of NAR in the mechanobiology of other cell types is well established [82–84]. The morphology of the cell nucleus is continuously modulated by various mechanical forces applied to the cell [83]. Changes in nuclear shape, influenced by cellular geometry and mechanical stress, significantly impact gene expression. For instance, cells cultured on different geometries, such as elongated rectangles and small circles, exhibit distinct nuclear shapes. These variations lead to changes in gene expression due to alterations in nuclear architecture [85]. Altering the shape of the nucleus can disrupt the homeostasis between cell and nuclear mechanics [82], leading to irregular nuclear morphology and affecting the ability of the cell to generate force and follow chemical gradients. This disruption can influence gene expression, particularly of proteins associated with cell migration. Such changes are crucial in physiological processes like wound healing and immune response and pathophysiological conditions such as cancer metastasis [86]. Considering such an important role of nuclear mechanobiology in cell function, it was not surprising to observe micro-structurally dependent changes in nuclear shape in VIC, a cell type that is subjected to high levels of macro-scale scale strains during opening and closure of the valve leaflets [77,87].

A more detailed analysis of our experimental data revealed a consistent alignment of cell nuclei with the surrounding collagen [88]. Such an observation was consistent with previously published work [36]. Given the complexity of the deformation of an entire cell (including the membrane and cytoplasm in addition to that of the nucleus) within intact tissues, NAR as a measurement of overall cellular deformation was deemed a more appropriate metric. However, it should be noted that exclusion of intracellular structure and organelles from the computational model was a limiting factor in our study.

A key aspect of our modeling approach was our ability to examine cells in different orientations relative to the ECM fiber architecture. Such a strategy has the potential for a more nuanced understanding of how cellular orientation and ECM structure interplay in determining cell deformation and valve mechanics. We examined the NAR alteration under equibiaxial mechanical loading in four different scenarios pertaining to the initial population of the cell nuclei (Table 1). As shown in Fig. 6, an initial rapid increase in NAR, followed by a more gradual rise, was most probably due to the decreased undulation of ECM fibers and the eventual full recruitment of collagen, for all four scenarios. Such an observation was consistent with trends in prior experimental studies in soft tissues (e.g., refer to the study of Foong et al. in the corneoscleral shell [89]). It also underscores the predictive capability of our computational model in simulating the biomechanical behavior of fiber networks under different loading levels. In our computational approach (Fig. 6), we primarily focused on the responses of a cell population, as this method seemed most relevant for comparison with experimental data. Interestingly, the mean responses of the nuclei under increasing stress were similar across all four simulated scenarios and aligned with the experimental outcomes. These responses, characterized by an initial rapid rise followed by a slower increase, were consistent with the observations of Lee et al. in mitral valve leaflets [90].

It should be noted, however, that the computational model has the capability of providing detailed information for individual cells, which is valuable for understanding the multi-scale mechanobiology of the VIC. For example, Fig. 7 shows the comparative deformation of two nuclei with the same initial shape, exposed to identical macro-scale mechanical loading. However, the network in Fig. 7(*a*) consisted of fibers primarily aligned with the circumferential direction of the leaflet, whereas the network in Fig. 7(*b*) had fibers predominantly aligned in the radial direction (i.e., perpendicular to those in Fig. 7(*a*)). In other words, the nucleus in Fig. 7(*a*) was aligned with the main fiber direction, whereas the nucleus in Fig. 7(*b*) had its main axis perpendicular to the main fiber direction. The comparison of loading-induced changes in the NAR is intriguing. In the case of Fig. 7(*a*), the NAR initially increased rapidly before the rate of increase slowed down. Conversely, in the case shown in Fig. 7(*b*), the changes in NAR were much smaller, and it appeared that the NAR did not change with loading after a certain point. This differential behavior between the two fiber networks underscores the significance of ECM fiber alignment in dictating the mechanical response of the cell nuclei. The link between macro-scale mechanical loading and ECM collagen remodeling has been well established [91,92]. The aforementioned example illustrates how such changes in the ECM network could be *directly* linked to nuclear mechanobiology.

Finally, the interdependency between VIC NAR and macro-scale mechanical loading is of great importance, as heart valves

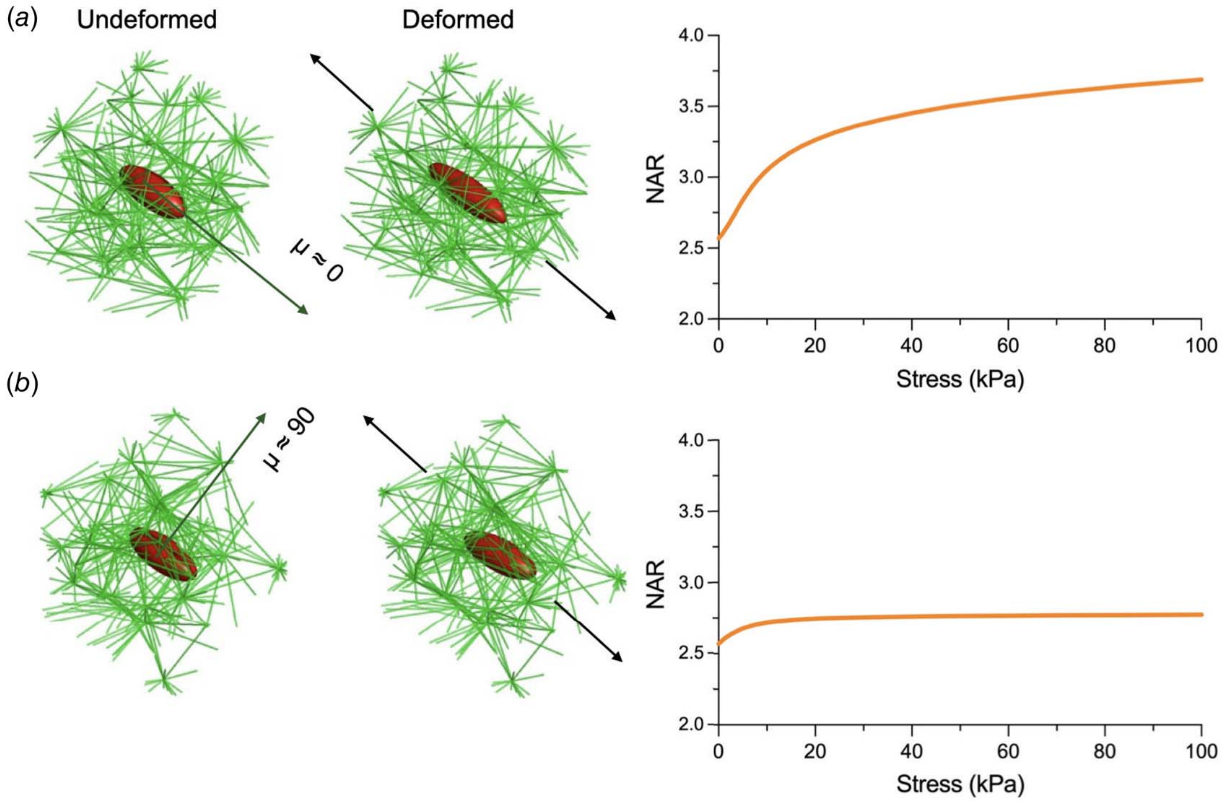

Fig. 7 Comparison of the nuclear deformation simulation in two networks with different mean fiber orientations. The figure depicts the NAR changes, within a representative fiber element (RVE): (*a*) The fibers in the RVE are mainly aligned circumferentially and (*b*) RVE fibers are mainly aligned radially. Both models have identical macro-scale mechanical loading in the circumferential direction. The macro-scale model is not shown.

experience significant cyclic mechanical strain throughout an individual's life. In our previous in vivo studies, we demonstrated how surgical procedures such as ring annuloplasty could drastically alter the macro-scale deformation of the mitral valve anterior leaflet in an ovine model [93]. Our current modeling suggests that the deformation of VIC nuclei in the tricuspid valve would be altered during each cardiac cycle when macro-scale loading is changed from that of a healthy valve, following surgical procedures such as ring annuloplasty.

Our study was not without limitations. The discrepancy between the model and the experimental data could stem from several factors. The anisotropic contribution of the intricate intracellular structure was not included in the computational model. In this study, we assumed that nuclei undergo affine deformation in correspondence with the positional changes of the ECM at the focal adhesion point within each representative volume element. Our model can be improved upon by the addition of the non-affine deformation of the intracellular structure such as actin microfilaments, microtubules, and/or intermediate filaments. Moreover, it has been shown that nuclear properties vary by leaflet and depth in similar ways that collagen orientation varies by leaflet and depth [36,88]. Our simulation, however, assumed similar structure along the thickness of the valve. Another limitation of our experimental approach was the inability to image the same leaflet under different mechanical loads. Utilizing imaging techniques that allow for the mechanical deformation of the valve while being imaged (e.g., see Ref. [94]) could better represent the load-dependent deformation of the nuclei. Despite such limitations, we found reasonable agreement between the outcomes of the computational model and the experiments.

5 Conclusions

In this study, we conducted a comprehensive analysis of the impact of mechanical loading on nuclei deformation in the TV anterior leaflet. Our observations revealed a notable influence of mechanical forces on nuclear shape, with significant changes in average NAR potentially triggering deviations in gene expression and protein synthesis. We also identified a relation between the orientation of collagen fibers and the NAR of VICs. Our findings highlight the importance of considering ECM fiber alignment in future studies of valve biomechanics to develop more accurate models for predicting cellular responses to mechanical stimuli. Overall, our study highlights the complex interplay between the mechanical environment of the valve and the cellular responses, providing insights into how mechanical forces impact the health and function of the tricuspid valve.

Acknowledgment

The authors acknowledge the funding provided for this work by the National Science Foundation (NSF CAREER Award 2049088). They also recognize the computational facilities from Research Computing at Northeastern University. The use of the research computing reserved cluster from Sinan Müftü is gratefully acknowledged. The authors also thank the Institute for Chemical Imaging of Living Systems at Northeastern University for consultation and imaging support.

Conflict of Interest

This article does not include research in which human participants were involved. Informed consent not applicable. This article does not include any research in which animal participants were involved.

Data Availability Statement

The datasets generated and supporting the findings of this article are obtainable from the corresponding author upon reasonable request.

Nomenclature

f = fiber axial force
v = ellipsoid center
$\hat{x}$ = ellipsoid surface
$\bar{y}$ = experimental measurement mean
$\hat{y}$ = simulated measurement
$\boldsymbol{a}$ = cell nuclei tertiary axis
$\boldsymbol{b}$ = cell nuclei secondary axis
$\boldsymbol{c}$ = cell nuclei primary axis
G = shear modulus
J = deformation gradient tensor determinant
L = total fiber length
V = volume
f_j = boundary cross-link force in j-direction
n_k = RVE surface normal vector
r_i = fiber direction unit vector
s_{ij} = microscopic volume-averaged Cauchy stress tensor
$u_{k,i}$ = displacement gradient
y_i = experimental measurement
A_f = mean fiber cross-sectional area
B_{ij} = left Cauchy–Green deformation tensor
D_{ij} = ellipsoid shape tensor
E_f = dimensionless fiber stiffness parameter
F_{ij} = deformation gradient tensor
H_{ij} = orientation tensor
Q_{ij} = eigenvector matrix
$\boldsymbol{e}^{(i)}$ = SALS reference frame vectors
R^2 = coefficient of determination
V' = non-dimensionalized volume
$V^{(i)}$ = ellipsoid eigenvector
$w_i^{(k)}$ = orientation tensor eigenvalue
x_i' = boundary cross-link position
S_{ij}' = macroscopic volume-averaged Cauchy stress tensor
S_{ij}^m = matrix stress tensor

Greek Symbols

α = anisotropy index
β = dimensionless nonlinearity parameter
γ = RVE edge length
δ_{ij} = Kronecker delta function
ε_G = fiber Green strain
ε_G^c = critical fiber Green strain
θ = fiber direction
Λ_{ij} = diagonal eigenvalue matrix
$\lambda^{(i)}$ = orientation tensor eigenvector
λ_f^c = critical stretch
λ_f = fiber stretch
μ = primary fiber direction
ν = Poisson's ratio
ψ = fiber volume fraction

Abbreviations

ECM = extracellular matrix
FE = finite element
NAR = nuclear aspect ratio
PBS = phosphate buffered saline
RVE = representative volume element
SALS = small angle light scattering
TV = tricuspid valve
VIC = valve interstitial cell

Appendix

To further extend the impact of our research and in line with our prior efforts [7,44,95–98], we have created an educational component related to the findings presented in this paper. In this appendix, we include a learning exercise suitable for a graduate-level introductory course in biomechanics or continuum mechanics.

Problem—Approximate changes in the NAR by assuming that the nuclear shape deforms affinely with the macro-scale tissue deformation. As a first approximation, consider a two-dimensional shape (i.e., an ellipse) for the nuclei with an initial NAR of 2.57. Use the experimental data for tissue-level tension and displacement provided in Fig. 4 for a 7 mm × 7 mm × 0.432 mm sample. Compare your results with the mean of the experimental and computational outcomes presented in Fig. 6.

References

[1] Dreyfus, J., Flagiello, M., Bazire, B., Eggenspieler, F., Viau, F., Riant, E., Mbaki, Y., et al., 2020, "Isolated Tricuspid Valve Surgery: Impact of Aetiology and Clinical Presentation on Outcomes," Eur. Heart J., **41**(45), pp. 4304–4317.

[2] Lee, J.-W., Song, J.-M., Park, J. P., Lee, J. W., Kang, D.-H., and Song, J.-K., 2010, "Long-Term Prognosis of Isolated Significant Tricuspid Regurgitation," Circ. J., **74**(2), pp. 375–380.

[3] Guenther, T., Noebauer, C., Mazzitelli, D., Busch, R., Tassani-Prell, P., and Lange, R., 2008, "Tricuspid Valve Surgery: A Thirty-Year Assessment of Early and Late Outcome," Eur. J. Cardiothorac. Surg., **34**(2), pp. 402–409.

[4] Jeganathan, R., Armstrong, S., Al-Alao, B., and David, T., 2013, "The Risk and Outcomes of Reoperative Tricuspid Valve Surgery," Ann. Thorac. Surg., **95**(1), pp. 119–124.

[5] Kwon, D.-A., Park, J.-S., Chang, H.-J., Kim, Y.-J., Sohn, D.-W., Kim, K.-B., Ahn, H., Oh, B.-H., Park, Y.-B., and Choi, Y.-S., 2006, "Prediction of Outcome in Patients Undergoing Surgery for Severe Tricuspid Regurgitation Following Mitral Valve Surgery and Role of Tricuspid Annular Systolic Velocity," Am. J. Cardiol., **98**(5), pp. 659–661.

[6] Pfannmüller, B., Moz, M., Misfeld, M., Borger, M. A., Funkat, A.-K., Garbade, J., and Mohr, F. W., 2013, "Isolated Tricuspid Valve Surgery in Patients With Previous Cardiac Surgery," J. Thorac. Cardiovasc. Surg., **146**(4), pp. 841–847.

[7] Thomas, V. S., Lai, V., and Amini, R., 2019, "A Computational Multi-scale Approach to Investigate Mechanically-Induced Changes in Tricuspid Valve Anterior Leaflet Microstructure," Acta Biomater., **94**, pp. 524–535.

[8] Pant, A. D., Thomas, V. S., Black, A. L., Verba, T., Lesicko, J. G., and Amini, R., 2018, "Pressure-Induced Microstructural Changes in Porcine Tricuspid Valve Leaflets," Acta Biomater., **67**, pp. 248–258.

[9] Sadeghinia, M. J., Aguilera, H. M., Urheim, S., Persson, R. M., Ellensen, V. S., Haaverstad, R., Holzapfel, G. A., Skallerud, B., and Prot, V., 2023, "Mechanical Behavior and Collagen Structure of Degenerative Mitral Valve Leaflets and a Finite Element Model of Primary Mitral Regurgitation," Acta Biomater., **164**, pp. 269–281.

[10] Chen, J.-H., and Simmons, C. A., 2011, "Cell–Matrix Interactions in the Pathobiology of Calcific Aortic Valve Disease: Critical Roles for Matricellular, Matricrine, and Matrix Mechanics Cues," Circ. Res., **108**(12), pp. 1510–1524.

[11] Green, E. M., Mansfield, J. C., Bell, J. S., and Winlove, C. P., 2014, "The Structure and Micromechanics of Elastic Tissue," Interface Focus, **4**(2), p. 20130058.

[12] Rosenbloom, J., Koo, H., Howard, P. S., Mecham, R., and Macarak, E. J., 1995, *Elastic Fibers and Their Role in Bladder Extracellular Matrix*, Springer US, Boston, MA, pp. 161–172.

[13] Pyeritz, R. E., 2000, "The Marfan Syndrome," Annu. Rev. Med., **51**(1), pp. 481–510.

[14] Kelleher, C. M., McLean, S. E., and Mecham, R. P., 2004, "Vascular Extracellular Matrix and Aortic Development," *Developmental Vascular Biology*, Current Topics in Developmental Biology, G. P. Schatten, ed., Vol. 62, Academic Press, Amsterdam, Netherlands, pp. 153–188.

[15] Ramirez, F., and Dietz, H. C., 2009, "Extracellular Microfibrils in Vertebrate Development and Disease Processes," J. Biol. Chem., **284**(22), pp. 14677–14681.

[16] Schoen, F. J., 2008, "Evolving Concepts of Cardiac Valve Dynamics," Circulation, **118**(18), pp. 1864–1880.

[17] Ammash, N. M., Sundt, T. M., and Connolly, H. M., 2008, "Marfan Syndrome–Diagnosis and Management," Curr. Probl. Cardiol., **33**(1), pp. 7–39.

[18] Mascherbauer, J., and Maurer, G., 2010, "The Forgotten Valve: Lessons to Be Learned in Tricuspid Regurgitation," Eur. Heart J., **31**(23), pp. 2841–2843.

[19] Fung, Y., 1981, "The Lung—A Perspective of Biomechanics Development," ASME J. Biomech. Eng., **103**(2), pp. 91–96.

[20] Taylor, P., 2003, "The Cardiac Valve Interstitial Cell," Int. J. Biochem. Cell Biol., **35**(2), pp. 113–118.

[21] Dobner, S., Amadi, O. C., and Lee, R. T., 2012, "Chapter 14—Cardiovascular Mechanotransduction," *Muscle*, J. A. Hill and E. N. Olson, eds., Academic Press, Boston, MA/Waltham, MA, pp. 173–186.

[22] Fayet, C., Bendeck, M. P., and Gotlieb, A. I., 2007, "Cardiac Valve Interstitial Cells Secrete Fibronectin and Form Fibrillar Adhesions in Response to Injury," Cardiovasc. Pathol., **16**(4), pp. 203–211.

[23] Katz, B.-Z., Zamir, E., Bershadsky, A., Kam, Z., Yamada, K. M., and Geiger, B., 2000, "Physical State of the Extracellular Matrix Regulates the Structure and Molecular Composition of Cell–Matrix Adhesions," Mol. Biol. Cell, **11**(3), pp. 1047–1060.

[24] Zamir, E., and Geiger, B., 2001, "Components of Cell–Matrix Adhesions," J. Cell Sci., **114**(20), pp. 3577–3579.

[25] Geiger, B., and Bershadsky, A., 2001, "Assembly and Mechanosensory Function of Focal Contacts," Curr. Opin. Cell Biol., **13**(5), pp. 584–592.

[26] Sastry, S. K., and Burridge, K., 2000, "Focal Adhesions: A Nexus for Intracellular Signaling and Cytoskeletal Dynamics," Exp. Cell Res., **261**(1), pp. 25–36.

[27] Wang, H., Leinwand, L. A., and Anseth, K. S., 2014, "Cardiac Valve Cells and Their Microenvironment—Insights From In Vitro Studies," Nat. Rev. Cardiol., **11**(12), pp. 715–727.

[28] Hayakawa, K., Tatsumi, H., and Sokabe, M., 2012, "Mechano-sensing by Actin Filaments and Focal Adhesion Proteins," Commun. Integr. Biol., **5**(6), pp. 572–577.

[29] Seong, J., Wang, N., and Wang, Y., 2013, "Mechanotransduction at Focal Adhesions: From Physiology to Cancer Development," J. Cell Mol. Med., **17**(5), pp. 597–604.

[30] Lomakin, A. J., Cattin, C. J., Cuvelier, D., Alraies, Z., Molina, M., Nader, G. P. F., Srivastava, N., et al., 2020, "The Nucleus Acts as a Ruler Tailoring Cell Responses to Spatial Constraints," Science, **370**(6514), p. eaba2894.

[31] Venturini, V., Pezzano, F., Castro, F. C., Häkkinen, H.-M., Jiménez-Delgado, S., Colomer-Rosell, M., Marro, M., et al., 2020, "The Nucleus Measures Shape Changes for Cellular Proprioception to Control Dynamic Cell Behavior," Science, **370**(6514), p. eaba2644.

[32] Ku, C.-H., Johnson, P. H., Batten, P., Sarathchandra, P., Chambers, R. C., Taylor, P. M., Yacoub, M. H., and Chester, A. H., 2006, "Collagen Synthesis by Mesenchymal Stem Cells and Aortic Valve Interstitial Cells in Response to Mechanical Stretch," Cardiovasc. Res., **71**(3), pp. 548–556.

[33] Lacerda, C. M., MacLea, H. B., Kisiday, J. D., and Orton, E. C., 2012, "Static and Cyclic Tensile Strain Induce Myxomatous Effector Proteins and Serotonin in Canine Mitral Valves," J. Vet. Cardiol., **14**(1), pp. 223–230.

[34] Stevanella, M., Votta, E., Lemma, M., Antona, C., and Redaelli, A., 2010, "Finite Element Modelling of the Tricuspid Valve: A Preliminary Study," Med. Eng. Phys., **32**(10), pp. 1213–1223.

[35] Kong, F., Pham, T., Martin, C., McKay, R., Primiano, C., Hashim, S., Kodali, S., and Sun, W., 2018, "Finite Element Analysis of Tricuspid Valve Deformation From Multi-slice Computed Tomography Images," Ann. Biomed. Eng., **46**(8), pp. 1112–1127.

[36] Meador, W. D., Mathur, M., Sugerman, G. P., Jazwiec, T., Malinowski, M., Bersi, M. R., Timek, T. A., and Rausch, M. K., 2020, "A Detailed Mechanical and Microstructural Analysis of Ovine Tricuspid Valve Leaflets," Acta Biomater., **102**, pp. 100–113.

[37] Kamensky, D., Xu, F., Lee, C.-H., Yan, J., Bazilevs, Y., and Hsu, M.-C., 2018, "A Contact Formulation Based on a Volumetric Potential: Application to Isogeometric Simulations of Atrioventricular Valves," Comput. Methods Appl. Mech. Eng., **330**, pp. 522–546.

[38] Laurence, D., Ross, C., Jett, S., Johns, C., Echols, A., Baumwart, R., and Towner, R., 2019, "An Investigation of Regional Variations in the Biaxial Mechanical Properties and Stress Relaxation Behaviors of Porcine Atrioventricular Heart Valve Leaflets," J. Biomech., **83**, pp. 16–27.

[39] Khoiy, K. A., Abdulhai, S., Glenn, I. C., Ponsky, T. A., and Amini, R., 2018, "Anisotropic and Nonlinear Biaxial Mechanical Response of Porcine Small Bowel Mesentery," J. Mech. Behav. Biomed. Mater., **78**(Supplement C), pp. 154–163.

[40] Amini Khoiy, K., and Amini, R., 2016, "On the Biaxial Mechanical Response of Porcine Tricuspid Valve Leaflets," ASME J. Biomech. Eng., **138**(10), p. 104504.

[41] Salinas, S. D., Clark, M. M., and Amini, R., 2019, "Mechanical Response Changes in Porcine Tricuspid Valve Anterior Leaflet Under Osmotic-Induced Swelling," Bioengineering, **6**(3), p. 70.

[42] Salinas, S. D., Clark, M. M., and Amini, R., 2020, "The Effects of –80 °C Short-Term Storage on the Mechanical Response of Tricuspid Valve Leaflets," J. Biomech., **98**, p. 109462.

[43] Salinas, S. D., Farra, Y. M., Amini Khoiy, K., Houston, J., Lee, C. -H., Bellini, C., and Amini, R., 2022, "The Role of Elastin on the Mechanical Properties of the Anterior Leaflet in Porcine Tricuspid Valves," PLoS One, **17**(5), pp. 1–24.

[44] Clarin, J., Dang, D., Santos, L., and Amini, R., 2023, "Mechanical Characterization of Porcine Tricuspid Valve Anterior Leaflets Over Time Applications to Ex Vivo Studies," ASME Open J. Eng., **2**, p. 021032.

[45] Rashidi, N., Pant, A. D., Salinas, S. D., Shah, M., Thomas, V. S., Zhang, G., Dorairaj, S., and Amini, R., 2021, "Iris Stromal Cell Nuclei Deform to More Elongated Shapes During Pharmacologically-Induced Miosis and Mydriasis," Exp. Eye Res., **202**, p. 108373.

[46] Lee, C.-H., Carruthers, C. A., Ayoub, S., Gorman, R. C., Gorman, J. H., and Sacks, M. S., 2015, "Quantification and Simulation of Layer-Specific Mitral Valve Interstitial Cells Deformation Under Physiological Loading," J. Theor. Biol., **373**, pp. 26–39.

[47] Carruthers, C. A., Alfieri, C. M., Joyce, E. M., Watkins, S. C., Yutzey, K. E., and Sacks, M. S., 2012, "Gene Expression and Collagen Fiber Micromechanical Interactions of the Semilunar Heart Valve Interstitial Cell," Cell Mol. Bioeng., **5**(3), pp. 254–265.

[48] Stella, J. A., Liao, J., Hong, Y., Merryman, W. D., Wagner, W. R., and Sacks, M. S., 2008, "Tissue-to-cCellular Level Deformation Coupling in Cell Micro-integrated Elastomeric Scaffolds," Biomaterials, **29**(22), pp. 3228–3236.

[49] Sacks, M. S., Smith, D. B., and Hiester, E. D., 1997, "A Small Angle Light Scattering Device for Planar Connective Tissue Microstructural Analysis," Ann. Biomed. Eng., **25**(4), pp. 678–689.

[50] Patil, P. S., Fathollahipour, S., Inmann, A., Pant, A., Amini, R., Shriver, L. P., and Leipzig, N. D., 2019, "Fluorinated Methacrylamide Chitosan Hydrogel Dressings Improve Regenerated Wound Tissue Quality in Diabetic Wound Healing," Adv. Wound Care, **8**(8), pp. 374–385.

[51] Thomas, V. S., Salinas, S. D., Pant, A. D., Dorairaj, S. K., and Amini, R., 2020, "Biomechanical Assessment of the Iris in Relation to Angle-Closure Glaucoma: A Multi-scale Computational Approach," *Lecture Notes in Computational Vision*

and Biomechanics, J. M. R. S. Tavares and R. N. Jorge, eds., Springer, Porto, Portugal, pp. 470–482.

[52] Advani, S., and Tucker, C., 1987, "The Use of Tensors to Describe and Predict Fiber Orientation in Short Fiber Composites," Trans. Soc. Rheol., **31**(8), pp. 751–784.

[53] Sander, E. A., and Barocas, V. H., 2009, "Comparison of 2D Fiber Network Orientation Measurement Methods," J. Biomed. Mater. Res. Part A, **88**(2), pp. 322–331.

[54] Chandran, P. L., and Barocas, V. H., 2006, "Deterministic Material-Based Averaging Theory Model of Collagen Gel Micromechanics," ASME J. Biomech. Eng., **129**(2), pp. 137–147.

[55] Stylianopoulos, T., and Barocas, V. H., 2007, "Volume-Averaging Theory for the Study of the Mechanics of Collagen Networks," Comput. Methods Appl. Mech. Eng., **196**(31–32), pp. 2981–2990.

[56] Hadi, M. F., Sander, E. A., and Barocas, V. H., 2012, "Multiscale Model Predicts Tissue-Level Failure From Collagen Fiber-Level Damage."

[57] Shah, S. B., Witzenburg, C., Hadi, M. F., Wagner, H. P., Goodrich, J. M., Alford, P. W., and Barocas, V. H., 2014, "Prefailure and Failure Mechanics of the Porcine Ascending Thoracic Aorta: Experiments and a Multiscale Model," ASME J. Biomech. Eng., **136**(2), p. 021028.

[58] Mahutga, R. R., Barocas, V. H., and Alford, P. W., 2023, "The Non-affine Fiber Network Solver: A Multiscale Fiber Network Material Model for Finite-Element Analysis," J. Mech. Behav. Biomed. Mater., **144**, pp. 105–967.

[59] De Jesus, A. M., Aghvami, M., and Sander, E. A., 2016, "A Combined In Vitro Imaging and Multi-scale Modeling System for Studying the Role of Cell Matrix Interactions in Cutaneous Wound Healing," PLoS One, **11**(2, p. e0148254.

[60] Witt, N. J., Woessner, A. E., Quinn, K. P., and Sander, E. A., 2022, "Multiscale Computational Model Predicts Mouse Skin Kinematics Under Tensile Loading," ASME J. Biomech. Eng., **144**(4), p. 041008.

[61] Hadi, M., Sander, E., Ruberti, J., and Barocas, V., 2012, "Simulated Remodeling of Loaded Collagen Networks Via Strain-Dependent Enzymatic Degradation and Constant-Rate Fiber Growth," Mech. Mater., **44**, pp. 72–82.

[62] Sander, E. A., Stylianopoulos, T., Tranquillo, R. T., and Barocas, V. H., 2009, "Image-Based Multiscale Modeling Predicts Tissue-Level and Network-Level Fiber Reorganization in Stretched Cell-Compacted Collagen Gels," Proc. Natl. Acad. Sci. U S A, **106**(42), pp. 17675–17680.

[63] Nemat-Nasser, S., and Hori, M., 2013, *Micromechanics: Overall Properties of Heterogeneous Materials*, Vol. 63, Elsevier, Springer New York, p. 561.

[64] Billiar, K. L., and Sacks, M. S., 2000, "Biaxial Mechanical Properties of the Native and Glutaraldehyde-Treated Aortic Valve Cusp: Part II—A Structural Constitutive Model," ASME J. Biomech. Eng., **122**(4), pp. 327–335.

[65] Bonet, J., and Wood, R. D., 1997, *Nonlinear Continuum Mechanics for Finite Element Analysis*, Cambridge University Press, Cambridge, UK.

[66] Stylianopoulos, T., and Barocas, V. H., 2007, "Multiscale, Structure-Based Modeling for the Elastic Mechanical Behavior of Arterial Walls," ASME J. Biomech. Eng., **129**(4), pp. 611–618.

[67] Jouzdani, S., Amini, R., and Barocas, V. H., 2013, "Contribution of Different Anatomical and Physiologic Factors to Iris Contour and Anterior Chamber Angle Changes During Pupil Dilation: Theoretical Analysis," Invest. Ophthalmol. Visual Sci., **54**(4), pp. 2977–2984.

[68] Amini, R., Whitcomb, J. E., Al-Qaisi, M. K., Akkin, T., Jouzdani, S., Dorairaj, S., Prata, T., et al., 2012, "The Posterior Location of the Dilator Muscle Induces Anterior Iris Bowing During Dilation," Even Absence Pupillary Block, Invest. Ophthalmol. Visual Sci., **53**(3), pp. 1188–1194.

[69] Lee, C.-H., Amini, R., Sakamoto, Y., Carruthers, C. A., Aggarwal, A., Gorman, R. C., Gorman, J. H., and Sacks, M. S., 2015, *Mitral Valves: A Computational Framework*, Springer London, London, pp. 223–255.

[70] Grötschel, M., Lovász, L., and Schrijver, A., 2012, *Geometric Algorithms and Combinatorial Optimization*, Springer Science & Business Media, Berlin, Germany.

[71] D'Amore, A., Luketich, S. K., Raffa, G. M., Olia, S., Menallo, G., Mazzola, A., D'Accardi, F., Grunberg, T., Gu, X., and Pilato, M., 2018, "Heart Valve Scaffold Fabrication: Bioinspired Control of Macro-scale Morphology, Mechanics and Micro-structure," Biomaterials, **150**, pp. 25–37.

[72] Rego, B. V., and Sacks, M. S., 2017, "A Functionally Graded Material Model for the Transmural Stress Distribution of the Aortic Valve Leaflet," J. Biomech., **54**, pp. 88–95.

[73] Stephens, E. H., and Borger, M. A., 2014, ""Forgotten" Valve Or "Eigmatic" Valve? Further Insights Into the Tricuspid Valve in Patients Undergoing Mitral Valve Surgery," J. Thorac. Cardiovasc. Surg., **148**(5), pp. 1962–1964.

[74] Taramasso, M., Vanermen, H., Maisano, F., Guidotti, A., La Canna, G., and Alfieri, O., 2012, "The Growing Clinical Importance of Secondary Tricuspid Regurgitation," J. Am. Coll. Cardiol., **59**(8), pp. 703–710.

[75] Mangieri, A., Montalto, C., Pagnesi, M., Jabbour, R. J., Rodés-Cabau, J., Moat, N., Colombo, A., and Latib, A., 2017, "Mechanism and Implications of the Tricuspid Regurgitation: From the Pathophysiology to the Current and Future Therapeutic Options," Circ.: Cardiovasc. Intervent., **10**(7), p. e005043.

[76] Di Mauro, M., Bivona, A., Iacò, A. L., Contini, M., Gagliardi, M., Varone, E., Gallina, S., and Calafiore, A. M., 2009, "Mitral Valve Surgery for Functional Mitral Regurgitation: Prognostic Role of Tricuspid Regurgitation," Eur. J. Cardio-Thorac. Surg., **35**(4), pp. 635–640.

[77] Mathur, M., Jazwiec, T., Meador, W., Malinowski, M., Goehler, M., Ferguson, H., Timek, T., and Rausch, M., 2019, "Tricuspid Valve Leaflet Strains in the Beating Ovine Heart," Biomech. Model. Mechanobiol., **18**(5), pp. 1351–1361.

[78] Ross, C. J., Laurence, D. W., Aggarwal, A., Hsu, M. -C., Mir, A., Burkhart, H. M., and Lee, C. -H., 2024, "Bayesian Optimization-Based Inverse Finite Element Analysis for Atrioventricular Heart Valves," Ann. Biomed. Eng., **52**(3), pp. 611–626.

[79] Laurence, D. W., Wang, S., Xiao, R., Qian, J., Mir, A., Burkhart, H. M., Holzapfel, G. A., and Lee, C.-H., 2023, "An Investigation of How Specimen Dimensions Affect Biaxial Mechanical Characterizations With CellScale BioTester and Constitutive Modeling of Porcine Tricuspid Valve Leaflets," J. Biomech., **160**, pp. 111–829.

[80] Amini Khoiy, K., Asgarian, K. T., Loth, F., and Amini, R., 2018, "Dilation of Tricuspid Valve Annulus Immediately After Rupture of Chordae Tendineae in Ex-Vivo Porcine Hearts," PLoS One, **13**(11), p. e0206744.

[81] Khoiy, K. A., Pant, A. D., and Amini, R., 2018, "Quantification of Material Constants for a Phenomenological Constitutive Model of Porcine Tricuspid Valve Leaflets for Simulation Applications," ASME J. Biomech. Eng., **140**(9), p. 094503.

[82] Lavrushkina, S., Ovsyannikova, N., Yudina, A., Strelkova, O., Zhironkina, O., Perepelina, K., Malashicheva, A., and Kireev, I., 2019, "The Role of Mechanical Properties of the Nucleus in Maintaining Tissue Homeostasis," Cell Tissue Biol., **13**(3), pp. 237–241.

[83] Jones, M. L., Dahl, K. N., Lele, T. P., Conway, D. E., Shenoy, V., Ghosh, S., and Szczesny, S. E., 2022, "The Elephant in the Cell: Nuclear Mechanics and Mechanobiology," ASME J. Biomech. Eng., **144**(8), p. 080802.

[84] Caille, N., Thoumine, O., Tardy, Y., and Meister, J.-J., 2002, "Contribution of the Nucleus to the Mechanical Properties of Endothelial Cells," J. Biomech., **35**(2), pp. 177–187.

[85] Alisafaei, F., Jokhun, D. S., Shivashankar, G., and Shenoy, V. B., 2019, "Regulation of Nuclear Architecture, Mechanics, and Nucleocytoplasmic Shuttling of Epigenetic Factors by Cell Geometric Constraints," Proc. Natl. Acad. Sci. U S A, **116**(27), pp. 13200–13209.

[86] Forman, J., Hine, B., Kaonis, S., and Ghosh, S., 2024, "Inhibition of Chromatin Condensation Disrupts Planar Cell Migration," Nucleus, **15**(1), p. 2325961.

[87] Amini Khoiy, K., Biswas, D., Decker, T. N., Asgarian, K. T., Loth, F., and Amini, R., 2016, "Surface Strains of Porcine Tricuspid Valve Septal Leaflets Measured in Ex Vivo Beating Hearts," ASME J. Biomech. Eng., **138**(11), p. 111006.

[88] Salinas, S. D., 2022, "Multiscale Biomechanics and Mechanobiology of the Tricuspid Valve Leaflets," Ph.D. thesis, Northeastern University, Boston, MA.

[89] Foong, T. Y., Hua, Y., Amini, R., and Sigal, I. A., 2023, "Who Bears the Load? IOP-Induced Collagen Fiber Recruitment Over the Corneoscleral Shell," Exp. Eye Res., **230**, p. 109446.

[90] Lee, C.-H., Carruthers, C. A., Ayoub, S., Gorman, R. C., Gorman III, J. H., and Sacks, M. S., 2015, "Quantification and Simulation of Layer-Specific Mitral Valve Interstitial Cells Deformation Under Physiological Loading," J. Theor. Biol., **373**, pp. 26–39.

[91] Zareian, R., Church, K. P., Saeidi, N., Flynn, B. P., Beale, J. W., and Ruberti, J. W., 2010, "Probing Collagen/Enzyme Mechanochemistry in Native Tissue With Dynamic, Enzyme-Induced Creep," Langmuir, **26**(12), pp. 9917–9926.

[92] Stephens, E. H., Nguyen, T. C., Itoh, A., Ingels Jr, N. B., Miller, D. C., and Grande-Allen, K. J., 2008, "The Effects of Mitral Regurgitation Alone Are Sufficient for Leaflet Remodeling," Circulation, **118**(14_suppl_1), pp. S243–S249.

[93] Amini, R., Eckert, C. E., Koomalsingh, K., McGarvey, J., Minakawa, M., Gorman, J. H., Gorman, R. C., and Sacks, M. S., 2012, "On the In Vivo Deformation of the Mitral Valve Anterior Leaflet: Effects of Annular Geometry and Referential Configuration," Ann. Biomed. Eng., **40**(7), pp. 1455–1467.

[94] Fata, B., Carruthers, C. A., Gibson, G., Watkins, S. C., Gottlieb, D., Mayer, J. E., and Sacks, M. S., 2013, "Regional Structural and Biomechanical Alterations of the Ovine Main Pulmonary Artery During Postnatal Growth," J. Biomech. Eng., **135**(2021022.

[95] Nwotchouang, B. S. T., Eppelheimer, M. S., Biswas, D., Pahlavian, S. H., Zhong, X., Oshinski, J. N., Barrow, D. L., Amini, R., and Loth, F., 2021, "Accuracy of Cardiac-Induced Brain Motion Measurement Using Displacement-Encoding With Stimulated Echoes (DENSE) Magnetic Resonance Imaging (MRI): A Phantom Study," Magn. Res. Med., **85**(3), pp. 1237–1247.

[96] Vargas, A. I., Tarraf, S. A., Jennings, T., Bellini, C., and Amini, R., 2024, "Vascular Remodeling During Late-Gestation Pregnancy: An In-Vitro Assessment of the Murine Ascending Thoracic Aorta," J. Biomech. Eng., **146**(7), pp. 1–34.

[97] Vargas, A. I., Tarraf, S. A., Fitzgibbons, T. P., Bellini, C., and Amini, R., 2023, "Biomechanical Remodeling of the Murine Descending Thoracic Aorta During Late-Gestation Pregnancy," Curr. Res. Physiol., **6**, p. 100102.

[98] Sebastian, F., Vargas, A. I., Clarin, J., Hurgoi, A., and Amini, R., 2024, "Meta Data Analysis of Sex Distribution of Study Samples Reported in Summer Biomechanics, Bioengineering, and Biotransport Annual Conference Abstracts," ASME J. Biomech. Eng., **146**(6), p. 060906.